Signatures of Fermi surface topology change in the nodal-line semimetal $ZrSiSe_{1-x}Te_x$

Jiangpeng Song, Meng Song, and Zhihao Li
Anhui Province Key Laboratory of Condensed Matter Physics at Extreme Conditions, High Magnetic Field Laboratory, HFIPS, Chinese Academy of Sciences, Hefei 230031, China
and Department of Physics, University of Science and Technology of China, Hefei 230026, China

Jian Wang, Yihao Wang, Lei Zhang, Yuyan Han, Liang Cao,* and Yimin Xiong†
Anhui Province Key Laboratory of Condensed Matter Physics at Extreme Conditions, High Magnetic Field Laboratory, HFIPS, Chinese Academy of Sciences, Hefei 230031, China

Dayong Liu‡
Key Laboratory of Materials Physics, Institute of Solid State Physics, HFIPS, Chinese Academy of Sciences, Hefei 230031, China

(Received 29 January 2021; accepted 19 April 2021; published 29 April 2021)

The topological nodal-line semimetal (TNLS) ZrSiM (M = S, Se, Te) is a promising platform to study the TNLS phase by tuning chalcogens. In this work, we study the evolution of the Fermi surface (FS) by tuning the Se/Te ratio in $ZrSiSe_{1-x}Te_x$ compounds. Transport properties and magnetometry results present signatures of Fermi surface topology change by the sudden changes in symmetry and carrier densities, as well as singularity of FSs at the critical chemical potentials. A $2\frac{1}{2}$-order Lifshitz transition occurs when $0.20 \leqslant x \leqslant 0.33$. Another $3\frac{1}{2}$-order electron topological transition is revealed by a large diamagnetic anomaly of susceptibility at $x \sim 0.80$. In combination with first-principles calculations, this study reveals the vital roles of spin-orbit coupling, charge transfer, and shifts of the chemical potential in the evolution of FSs in this system. Our results demonstrate how the FSs evolve in $ZrSiSe_{1-x}Te_x$ compounds, providing fundamental clues for designing topological state switchable devices.

DOI: 10.1103/PhysRevB.103.165141

I. INTRODUCTION

ZrSiM (M = S, Se, Te), a family of topological nodal-line semimetals (TNLSs) [1–5], has attracted extensive attention due to its exfoliated structure, which makes its members candidates for exploring novel properties in low-dimensional topological devices as well as future applications in fermitronics [6,7]. ZrSiM has relatively simple electronic band structures in the vicinity of the Fermi level among TNLSs, such as $PbTaSe_2$ [3] and $PtSn_4$ [4,8]. Thus, ZrSiM is suited to understanding the properties of topological nodal-line fermions, such as the high density of states at the Fermi level [9–12]. The Dirac bands of ZrSiM have robust linear band dispersions up to ~2 eV, which is much larger than that of most Dirac and Weyl materials [13–15], providing a wide range of tunable electronic topological states. Moreover, the titanic angular magnetoresistance (AMR) observed in ZrSiM under applied magnetic field motivates researchers to design neoteric magnetic sensors and switches for industrial applications [16–18].

ZrSiS and ZrSiSe have similar electronic band structures with a narrow corrugated Fermi surface (FS) tube surrounding the band-contact line [14], whereas ZrSiTe presents different FSs with quasi-two-dimensional (quasi-2D) characters, as shown in Fig. 1. Replacing Se by Te results in the enhancement of spin-orbit coupling (SOC), a much larger c/a lattice ratio, and charge transfer, which are significant to the change in the band structure [19–22]. Consequently, the energy of the electronic bands shifts upwards or downwards, and some subtle crucial distinctions of the electronic bands between ZrSiSe and ZrSiTe are observed in the vicinity of the Fermi level, as shown in Figs. 1(a) and 1(b). Due to the shifts of the electronic bands, additional small electron-type pockets along the Z-R direction and around the X point as well as hole-type pockets along the A-Z and M-Γ directions emerge in ZrSiTe, which have been reported in previous angle-resolved photoemission spectroscopy experiments [19]. Furthermore, there is a Dirac nodal line protected by nonsymmorphic symmetry along XR in the Fermi surface, as shown in Fig. 1(d). On the other hand, compared with ZrSiSe, the relatively stronger SOC and charge transfer in ZrSiTe lead to a larger band gap and energy shifts of the band-contact line. In Fig. 1(d), the locations where the topology of FSs changes are highlighted by colored circles in three-dimensional (3D) plot of ZrSiTe's FS. The distinct changes in FS topology (electron topological transitions) are closely related to the transport behaviors at low temperature [23]. Therefore, their transport properties show obvious differences, for example, the upturn behavior in the temperature dependence of the resistivity, and Shubnikov–de Haas (SdH) oscillations vanish

*lcao@hmfl.ac.cn
†yxiong@hmfl.ac.cn
‡dyliu@theory.issp.ac.cn

 ©2021 American Physical Society

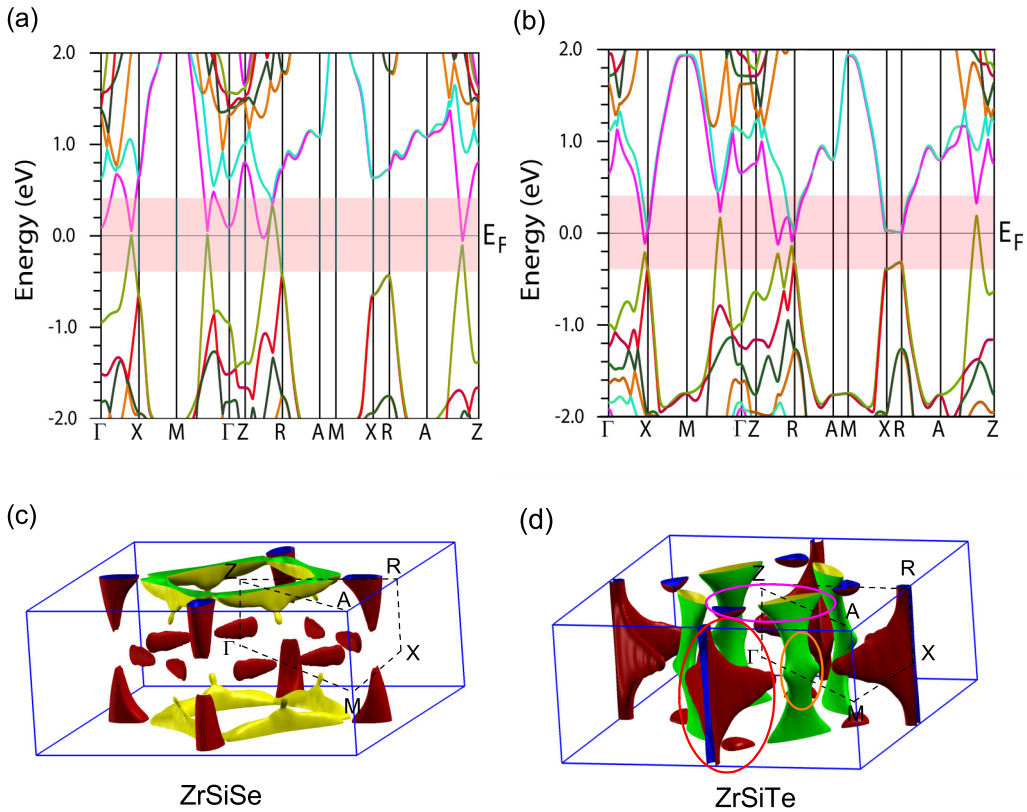

FIG. 1. (a) and (b) The calculated band structures of ZrSiSe and ZrSiTe with SOC. (c) and (d) The 3D plots of FSs of ZrSiSe and ZrSiTe. The major changes in FSs are highlighted by colored circles in (d).

in ZrSiTe up to 9 T due to its gapped-out nodal-line states [14,19]. Thus, ZrSi*M* is an ideal platform to study the tunable topological nodal-line states by regulating the lattice constant, SOC strength, and chemical potential [19,24].

A recent study demonstrated a temperature-induced Lifshitz transition in ZrSiSe due to the coeffect of SOC and excitonic instability [25]. Besides the temperature and pressure [26], theoretical and experimental investigations suggest that magnetic field H and chemical potential ζ tuned by chemical doping could cause changes in the FS topology in topological materials [23,27,28]. Moreover, according to theoretical predictions, if the chemical potential ζ passes through a singular point, such as a Dirac node, a higher-order electron topological transition occurs, accompanying the large anomaly in orbital susceptibility [23,29]. These raise a question about how the topology and geometry of FSs evolve in $ZrSiSe_{1-x}Te_x$ compounds. It is important to identify the role of lattice structure, nonsymmorphic symmetry-protected Dirac crossings, and SOC in the distinct difference of properties between ZrSiSe and ZrSiTe. Understanding the underlying mechanism of these changes will pave the way for designing practical topological switchable devices.

In this work, we synthesize a series of $ZrSiSe_{1-x}Te_x$ ($0 \leqslant x \leqslant 1$) compounds and present a detailed analysis of FSs by transport properties. On the basis of theoretical calculations, we clarify the evolution of the FS topology in $ZrSiSe_{1-x}Te_x$ compounds by changing the Se/Te ratio. Our findings suggest that there are two discontinuous transitions, including a $2\frac{1}{2}$-order Lifshitz transition occurring in the range $0.20 \leqslant x \leqslant 0.33$ and a $3\frac{1}{2}$-order electron topological transition occurring when $x \sim 0.80$. These results show signatures of FS topology change and clarify the details of FS evolution in nodal-line semimetal $ZrSiSe_{1-x}Te_x$.

II. EXPERIMENTAL METHODS

Platelike $ZrSiSe_{1-x}Te_x$ ($0 \leqslant x \leqslant 1$) single crystals were synthesized via the chemical vapor transport method [17]. The crystal structure was checked by x-ray diffraction (XRD) (Cu $K\alpha$ radiation) at room temperature. And chemical compositions were characterized by energy dispersive x-ray spectroscopy. The electrical transport measurements were performed by using the standard four-probe DC technique on an Oxford Instruments TeslatronPT cryogenic system. The resistivity was measured in the *ab* plane under both positive and negative magnetic fields to eliminate the factor of electrode asymmetry. The magnetization measurements were performed on a Quantum Design MPMS-3 system. The electronic structures of ZrSiSe and ZrSiTe were calculated by the first-principles calculations and the full-potential linearized augmented plane-wave method based on density functional theory as implemented in the WIEN2K code [30]. For the exchange and correlation potentials, the generalized gradient approximation of Perdew, Burke, and Ernzerhof [31] was used. A mesh of $35 \times 35 \times 15$ k-points was utilized for the full Brillouin zone. SOC was considered through a second variational procedure.

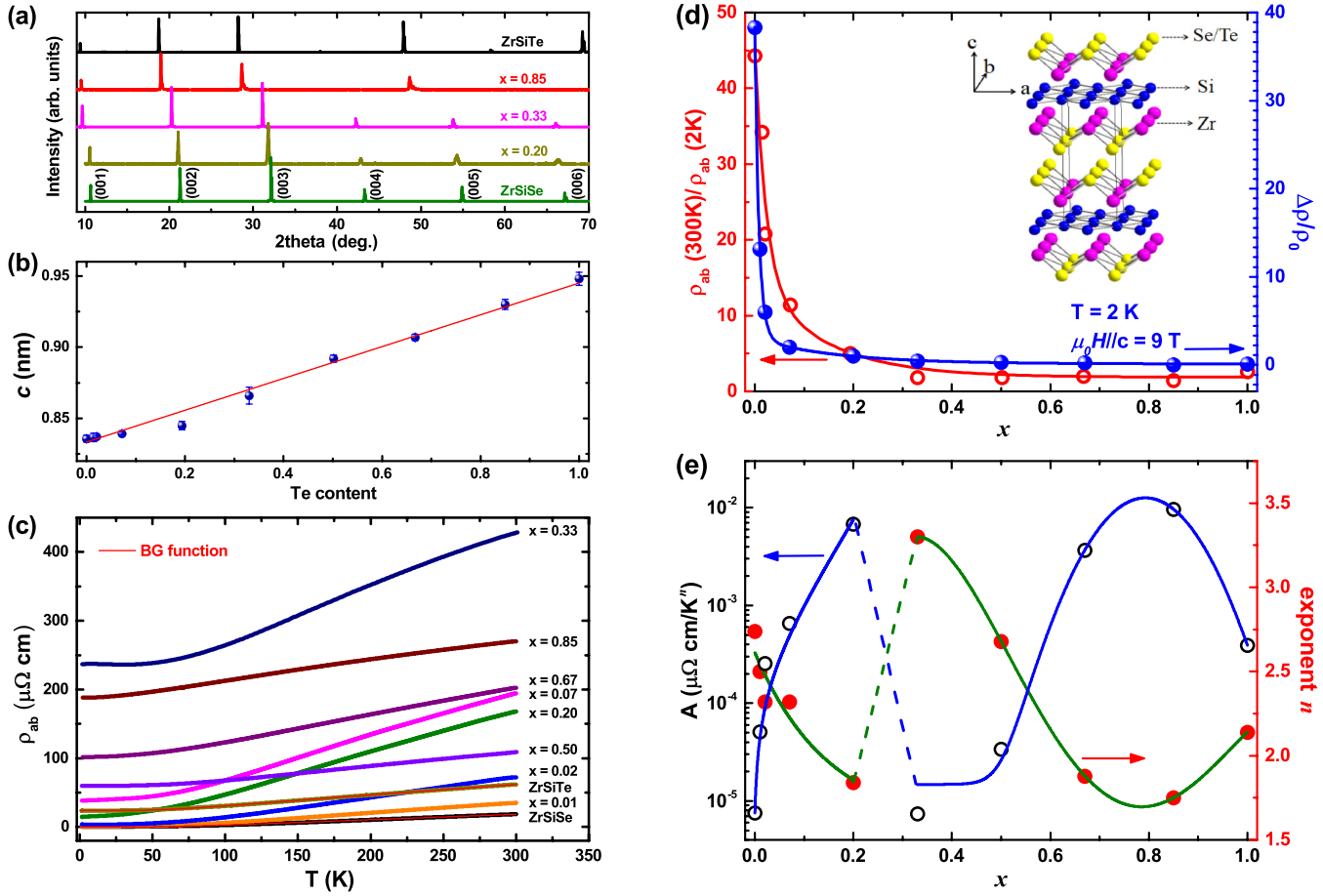

FIG. 2. (a) The XRD patterns of $ZrSiSe_{1-x}Te_x$ single crystals with indicated compositions. (b) The c-axis lattice parameters extracted from XRD patterns versus Te content. The red solid line represents a linear fit. Inset: the crystal structure of ZrSiSe/Te. (c) Temperature dependence of in-plane resistivity at zero field for $ZrSiSe_{1-x}Te_x$ samples. The red lines present the fit by the Bloch-Grüneisen function for ZrSiSe and ZrSiTe. (d) The residual resistivity ratio $\rho(300\,\mathrm{K})/\rho(2\,\mathrm{K})$ (red) and magnetoresistance $\Delta\rho/\rho_0$ (blue) under $\mu_0 H = 9$ T and $T = 2$ K of samples with various Te contents. (e) Parameters of power law fit of low-temperature resistivity ($\leqslant 100$ K) as a function of Te content.

III. RESULTS AND DISCUSSION

The crystal structure of ZrSiM [inset of Fig. 2(d)] belongs to the PbFCl-type structure with a Si square net layer sandwiched between two Zr-M layers along the c axis of the tetragonal unit cell [32]. Figure 2(a) shows the XRD patterns of single crystals with selected compositions; XRD spectra of all samples are shown in Fig. S1 of the Supplemental Material [33]. Only $(00l)$ Bragg peaks are observed, implying that the crystals are cleaved along the ab plane. The observed diffraction peaks show a systematic shift with the increase of Te content. The c-axis lattice parameters extracted from the $(00l)$ diffraction peaks via Bragg's law are plotted as a function of Te content in Fig. 2(b). It presents a linear dependence, indicating a systematic substitution of Se by Te. The temperature dependence of the in-plane resistivity ρ_{ab} for $ZrSiSe_{1-x}Te_x$ samples is plotted in Fig. 2(c). Over the entire temperature range, ZrSiSe and ZrSiTe both show metallic behavior and can be fitted by the Bloch-Grüneisen (BG) function including the Padé approximant for scattering due to electron-phonon coupling [34]. The Debye temperature Θ_R extracted from resistivity is about 482 K in ZrSiSe, which is comparable to 493 K in ZrSiS [35]. However, Θ_R of ZrSiTe is ~385 K, which is lower than those of ZrSiS and ZrSiSe and consistent with the weaker interlayer interactions in ZrSiTe [20]. The residual resistivity ratio [RRR $= \rho(300\,\mathrm{K})/\rho(2\,\mathrm{K})$] of the $ZrSiSe_{1-x}Te_x$ samples as a function of Te content is plotted in Fig. 2(d). It drops rapidly with the increase of Te content and changes systematically from 44.3 (of ZrSiSe) to 2.6 (of ZrSiTe). This is caused by the possible atomic disorder and lattice distortion induced by the mismatch between the Te atom and crystal structure [19]. Meanwhile, magnetoresistivity $\Delta\rho/\rho_0$ at 9 T and 2 K presents a Te content dependence similar to RRR, as shown in Fig. 2(d). The above-mentioned systematic evolution of the lattice structure and in-plane resistivity demonstrates that Te has substituted Se homogeneously. Although the RRR value decreases by more than an order of magnitude from ZrSiSe to ZrSiTe, electron-phonon coupling is still one of the dominant mechanisms of resistivity.

Low-temperature resistivity $\rho_{ab}(T)$ ($\leqslant 100$ K) of various samples with different Te contents can be well fitted by the power law expression $\rho(T) = \rho^* + AT^n$, where n is the exponent of the power law dependence. The extracted parameter A and exponent n of the indicated compounds are plotted in Fig. 2(e). For most samples, the exponent n is larger

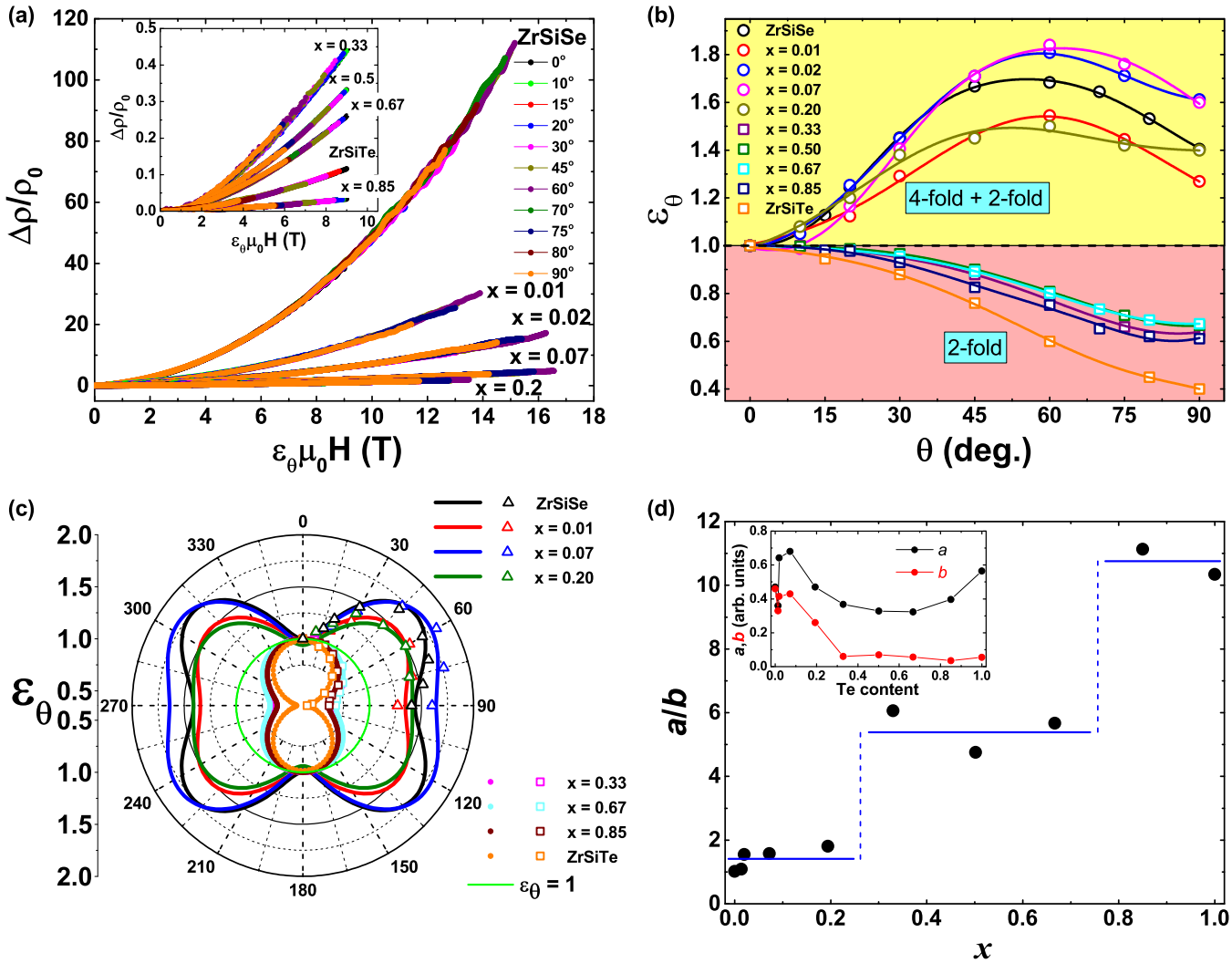

FIG. 3. (a) The scaling behavior of magnetoresistance at various angles and 2 K by using ε_θ for samples with the indicated Te content (all magnetoresistance data are as seen in Fig. S2). (b) ε_θ versus angle for various samples at 2 K. Symbols are extracted from corresponding experimental data. The regions of butterfly-shaped anisotropy and twofold anisotropy are highlighted in yellow and pink, respectively. (c) Polar plot of the angle dependence of ε_θ for selected samples at 2 K. Open triangle and square data points are extracted from corresponding experimental data, and colorful lines represent the fitting curves with $\varepsilon_\theta = a\sin^2(\theta) + b\sin^2(2\theta) + \delta$. (d) The ratio of a/b as a function of Te content. a and b are obtained from the fits in (b) and (c). Inset: a and b coefficients as a function of Te content.

than 2, indicating a non-Fermi-liquid temperature dependence of $\rho_{ab}(T)$, which is also less than 5 for the conventional electron-phonon coupling from the Bloch-Grüneisen law. This has been observed in the semimetals ZrSiS and LaBi (with $n \approx 3$) [13,36] and indicates that low-temperature resistivity is dominated by the interband *s-d* electron-phonon scattering instead of electron-electron scattering or intraband *s-s* electron-phonon scattering [37]. It is notable that both A and n present discontinuous changes between $x = 0.20$ and 0.33, denoted by the green and blue dashed lines. Meanwhile, another change in coefficients occurs around $x = 0.80$, as shown in Fig. 2(e). Because these parameters correspond to the character of FSs, these changes reflect a discontinuous evolution (topology change) of FSs between ZrSiSe and ZrSiTe.

To quantify FSs in $ZrSiSe_{1-x}Te_x$, MR versus applied magnetic field at 2 K and various angles are measured and scaled in a single curve by using the scaling factor ε_θ because the AMR value under 9 T cannot directly present the real situation of FSs in a nonperfectly compensated material [38–40]. The measured AMRs at 2 K as a function of the external field of each compound are plotted in Fig. S2. The external field is rotated in the plane perpendicular to the current, as shown in the sketch in Fig. S2. Figure 3(a) shows scaled AMR data for samples with the indicated compositions. ε_θ of different samples as a function of angle are presented to quantify the authentic geometry of their FSs, as shown in Fig. 3(b). For samples with $x \leqslant 0.20$, ε_θ increases with θ and reaches a maximum value at around 60°, then decreases. In these samples, ε_θ is always larger than 1, which indicates that ε_θ can be well characterized by a convolution of twofold and fourfold symmetries. However, for samples with $x \geqslant 0.33$, ε_θ decreases monotonically with θ; consequently, ε_θ is less than 1, indicating a twofold symmetry character of FSs in these compounds.

In order to analyze the relative weight of twofold and fourfold components, $\varepsilon_\theta = a\sin^2(\theta) + b\sin^2(2\theta) + \delta$ is used

to fit ε_θ in different samples, as shown in Fig. 3(c), where a is the coefficient of the twofold component, b is the coefficient of the fourfold component, and δ is an angle parameter [16]. The fitted curves show a butterfly pattern in compounds with $x \leqslant 0.20$, which are similar to those cases observed in ZrSiS and ZrSiSe [14]. For samples with $x \geqslant 0.33$, the symmetry of AMR data changes and shows a simple twofold character. The above change in the symmetry of the AMR results between $x = 0.20$ and 0.33 indicates a change in FS symmetry, which is in accordance with the discontinuous change in resistivity coefficients presented in Fig. 2(e).

The coefficients of twofold (a) and fourfold (b) symmetry components extracted from fits in Figs. 3(b) and 3(c) are plotted in the inset of Fig. 3(d). In order to analyze the evolution of FS geometry with changing Te content, the a/b ratio as a function of Te content is plotted in Fig. 3(d). The ratio a/b is about 1.5 when $x \leqslant 0.2$, indicating twofold and fourfold symmetries are equally important to the geometry of FS in these compounds. When x increases to 0.33, the ratio increases to about 6. This dramatic increase of a/b is consistent with the change in FSs as revealed by the AMR data. The average value of a/b is about 5 (when $0.33 \leqslant x \leqslant 0.67$), suggesting that the twofold symmetry becomes dominant. Another jump of a/b is observed around $x = 0.80$, indicating a further increase of the twofold symmetry character of FSs with the increase of Te content, which is in line with the change in resistivity coefficients observed in Fig. 2(e).

ZrSiM hosts two types of Dirac states: a nodal-line Dirac state and a 2D nonsymmorphic Dirac state near E_F [20,41]. The nodal-line Dirac state can be gapped by SOC, whereas the nonsymmorphic Dirac state is protected by the nonsymmorphic symmetry regardless of SOC strength. According to previous reports, the lattice parameter ratio of c/a in ZrSiM governs the energy shift of the nonsymmorphic Dirac cone [20]. The c/a ratios are ~2.27, ~2.31, and ~2.57 for ZrSiS, ZrSiSe, and ZrSiTe, respectively. Both ZrSiS and ZrSiSe have close values of the c/a ratio with a similar FS dimensionality, which is distinct from ZrSiTe, with a 2D-like character of FSs. In ZrSiS and ZrSiSe, the nonsymmorphic Dirac cone is far away from the Fermi level, as shown in Fig. 1(a) and hardly affects the transport properties. However, it is located very close to the Fermi level in ZrSiTe. Tuning M elements will modify lattice parameters, change SOC strength as well as chemical potential, and, consequently, affect the electronic structure of ZrSiM. Therefore, detailed investigations of transport properties of $ZrSiSe_{1-x}Te_x$ samples could provide clues to clarify the evolution of FSs from ZrSiSe to ZrSiTe.

Hall resistivity versus magnetic field is a useful probe to detect the properties of carriers and is often employed to identify the change in FSs. Hall resistivities of $ZrSiSe_{1-x}Te_x$ as a function of magnetic field at $T = 2$ K are displayed in Figs. 4(a) and 4(b). Field dependences of Hall resistivities are nonlinear, indicating the existence of multiple bands in $ZrSiSe_{1-x}Te_x$. The Hall conductivity $\sigma_{xy} = \rho_{xy}/(\rho_{xx}^2 + \rho_{xy}^2)$ is calculated by using the magnetic field dependence of the longitudinal resistivity $\rho_{xx}(H)$ and Hall resistivity $\rho_{xy}(H)$, as displayed in Figs. 4(c)–4(e). With increasing Te content, the Hall conductivity decreases by three orders of magnitude. Hall conductivity could be analyzed by using the two-carrier model, which was described in Refs. [14,25] for ZrSiSe and MoO_2 [25,42], respectively. The Hall conductivity tensor is given by [43]

$$\sigma_{xy} = \frac{e\mu_0 H n_1 \mu_1^2}{1 + \mu_1^2 \mu_0^2 H^2} - \frac{e\mu_0 H n_2 \mu_2^2}{1 + \mu_2^2 \mu_0^2 H^2}, \tag{1}$$

where n_1 and n_2 denote the carrier densities of two distinct bands and μ_1 and μ_2 denote the mobilities of carriers, respectively. The fits of $\sigma_{xy}(H)$ for $ZrSiSe_{1-x}Te_x$ with the indicated compositions are presented in Figs. 4(c)–4(e). The fitting curves are represented by red solid lines, which show good agreement with our experimental data in all compounds, demonstrating the coexistence of two types of carriers in all samples. According to the above two-carrier model, the carrier densities and mobilities of two distinct carriers are extracted and plotted in Figs. 4(f) and 4(g). As shown in Figs. 4(f) and 4(g), both carrier densities and mobilities exhibit a perfect electron-hole compensation in ZrSiSe, with hole and electron densities of $\pm 2.5 \times 10^{19}/\mathrm{cm}^3$ and mobilities of 1.38 and 1.08 $\times 10^4$ $\mathrm{cm}^2/\mathrm{V\,s}$, respectively. With the increase of Te content, carrier densities of both n_1 and n_2 decrease and reach an extremum of about $10^{16}/\mathrm{cm}^3$ at $x = 0.20$. Meanwhile, the type of carrier n_2 changes from an electron to a hole. In this Te content range, mobilities of two carriers also show different values [denoted by the green area in Fig. 4(g)]. The changes in carrier density and mobility could be an indication of change in FSs, which has been observed in ZrSiSe as a signature of temperature-induced Lifshitz transition [25]. Moreover, although only hole-type carriers are obtained by the fits of the two-carrier model in the samples for $x = 0.20$ and 0.33, the nonlinear dependence of Hall resistivities as a function of magnetic field [as seen in Figs. 4(a) and 4(b)] indicates the multiple-band nature of these samples. Thus, the change in carrier type provides further evidence for the topology change in FSs. With a further increase of Te content to 0.46 ($x \geqslant 0.46$), carrier densities restore the magnitude of $10^{19}/\mathrm{cm}^3$ and show an electron-hole compensation again. Meanwhile, the mobilities of two carriers are close to each other once again. Furthermore, the mobilities of carriers μ_1 and μ_2 decrease overall with increasing Te content because of the increase of SOC and lattice distortion. Although it is technically difficult to control the Te content very precisely, the above results demonstrate that a reconstruction of FSs occurs when x is between 0.20 and 0.33, which is consistent with our resistivity and AMR results.

SdH oscillations imply high mobility of the carriers and circumvent the geometric shape of the samples themselves to probe FSs. As shown in Figs. 5(a) and 5(b), SdH oscillations of $ZrSiSe_{0.98}Te_{0.02}$ are clearly observed in magnetoresistance data up to 9 T at 2 K because the Landau-quantized cylinders periodically cross the FSs under the increase of magnetic field. The oscillation amplitude decreases gradually with an increase of Te content and cannot be detected clearly when $x \geqslant 0.33$. To further probe the dimensionality of FSs in $ZrSiSe_{1-x}Te_x$, the frequencies at various angles are extracted to analyze using maximum entropy spectral analysis [44].

Figures 5(c) and 5(d) exhibit fast Fourier transform (FFT) spectra of SdH oscillations of $ZrSiSe_{0.98}Te_{0.02}$. FFT spectra of other samples show similar oscillation frequencies, as presented in Fig. S3. Five dominant frequencies (F_α, F_δ,

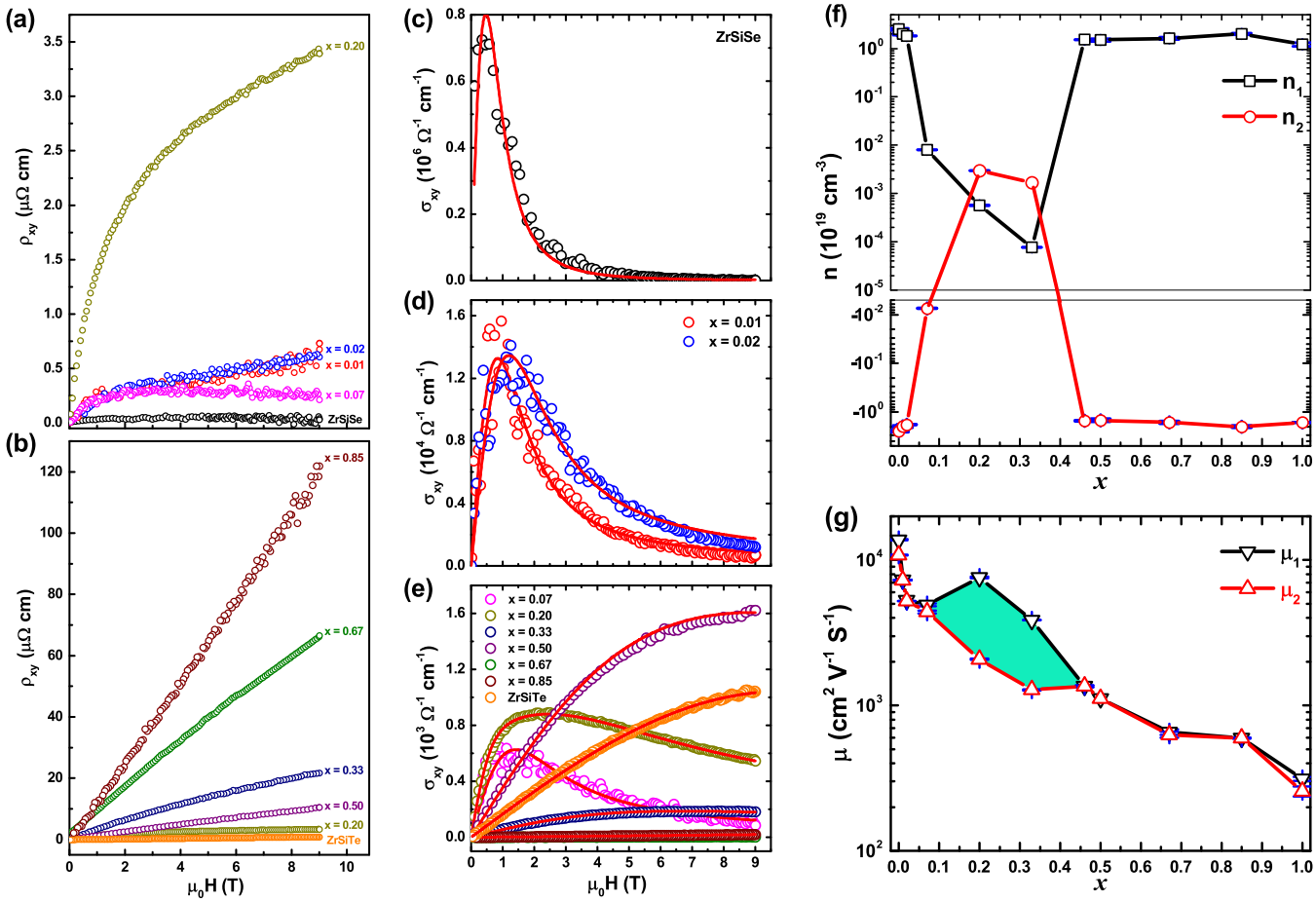

FIG. 4. (a) and (b) Hall resistivity curves of $ZrSiSe_{1-x}Te_x$ at $T = 2$ K. (c)–(e) Hall conductivity of $ZrSiSe_{1-x}Te_x$ at $T = 2$ K. (f) and (g) Carrier densities and mobilities of two carriers as a function of Te content.

F_ε, F_η, and F_β are used to denote the peak positions) show evident dependence of the angle, indicating quasi-2D characters of the corresponding FSs. Although the geometry of FSs in Fig. 1 is not ideal ellipsoids, an ellipsoid formula, $F(\theta) = F_0/\sqrt{\sin^2(\theta) + r^2\cos^2(\theta)}$ (r is the axial ratio of semimajor and semiminor axes in the ellipsoid), could still be employed to evaluate the dimensional information of each FS. As shown in Figs. 5(e) and 5(f), the angle dependence of F_α, F_ε, and F_β can be fitted well using the above ellipsoid formula, and extracted axial ratios as a function of Te content are plotted in Fig. 5(g). Axial ratios of the α and ε bands are independent of Te content when $x \leqslant 0.2$. However, the β band, which is highlighted by a red circle in Fig. 1(d), exhibits an evident composition dependence by increasing about 3 times, demonstrating an obvious change in FS geometry. Results for samples with greater Te substitution are absent because oscillations are not observed up to 9 T in these samples, as shown in Fig. S2.

Quantitative information for FSs also could be obtained from de Haas–van Alphen (dHvA) oscillations by magnetometry measurements [45]. Furthermore, the change in susceptibility (or magnetization) could serve as a signature of FS topology change in topological semimetals and semiconductors; for instance, for $Na_{1-x}Bi_x$ and BiTeI [29,46–50], their magnetic susceptibilities show a large diamagnetic anomaly when the chemical potential is tuned by doping and approaches band-crossing points or the band-contact line. Figure 6(a) presents the magnetization M versus magnetic field μ_0H curves of samples with the indicated composition under the magnetic field along the c axis and up to 7 T. The results measured under in-plane magnetic field present similar behavior and are shown in Fig. S4. Magnetization of the ZrSiSe single crystal was reported in a previous study by Hu *et al.* [14] and thus is not presented here. The inset in Fig. 6(a) shows M vs H data for $ZrSiSe_{0.99}Te_{0.01}$, which show diamagnetism up to 7 T and are the same as those of ZrSiSe. As shown in Fig. 6(a), diamagnetism is enhanced with increasing Te content and reaches the maximum value for $x = 0.67$. These curves show linear dependence with negative slope in a wide magnetic field range due to Landau diamagnetism, which becomes dominant in topological semimetals and semiconductors due to the low effective electron mass [50,51]. According to previous reports, for ZrSiSe and ZrSiTe, the effective cyclotron mass of carriers m^* is less than $0.1m_0$ [14], where m_0 is the free-electron mass. For sample $ZrSiSe_{0.99}Te_{0.01}$, the magnetic oscillations (dHvA) are observed at low temperature and high magnetic field, as shown in the inset in Fig. 6(a).

Strong dHvA oscillations and FFT spectra of in-plane magnetization at various temperatures are shown in Fig. 6(b).

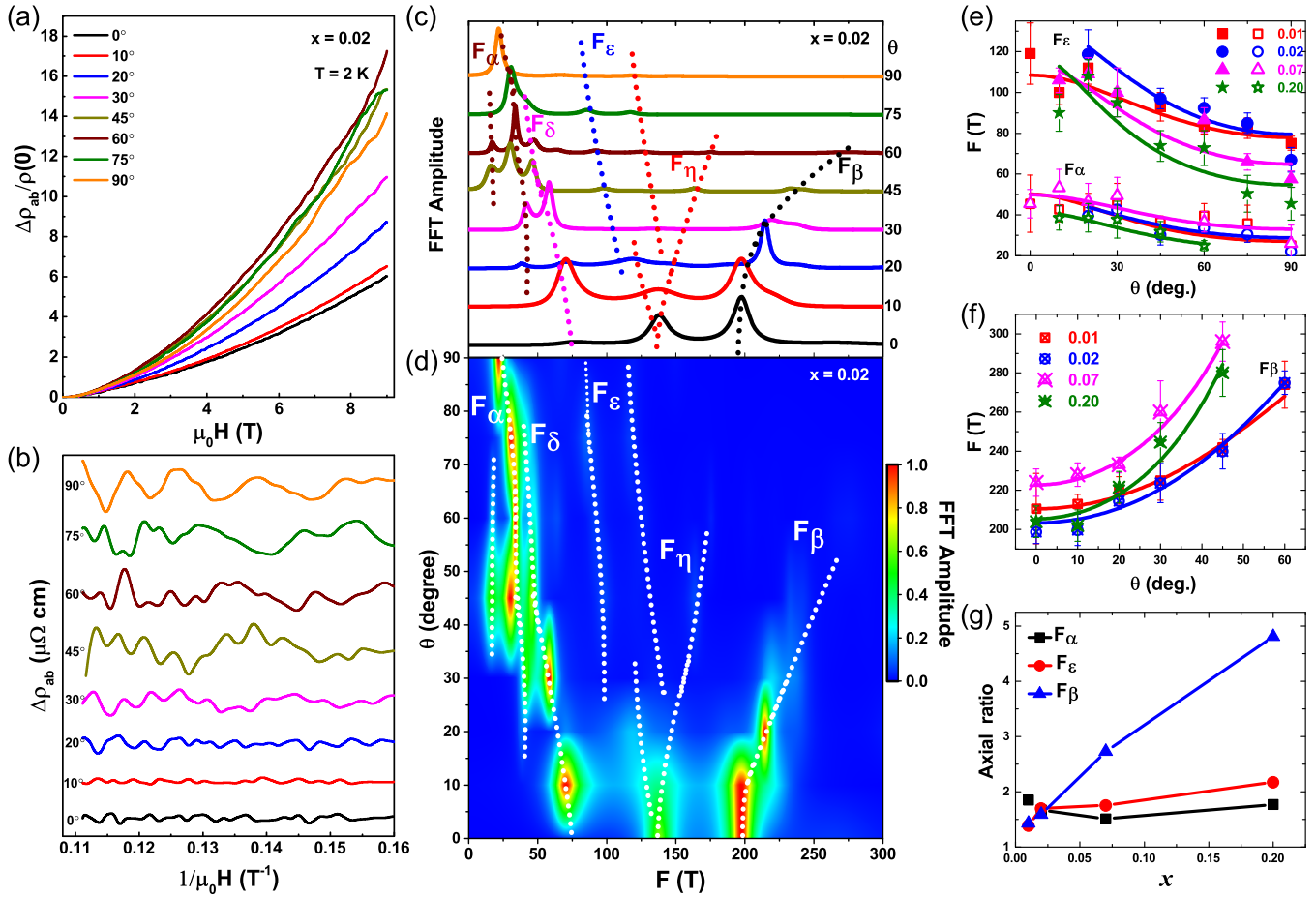

FIG. 5. (a) Field dependence of in-plane resistivity for $ZrSiSe_{0.98}Te_{0.02}$ with different field orientations. (b) The oscillatory part of in-plane resistivity $\Delta\rho_{ab}$ under different field orientations. (c) and (d) FFT spectra (SdH) and contour figure of the oscillatory components extracted from AMR data for $ZrSiSe_{0.98}Te_{0.02}$. (e) and (f) Angle dependence of oscillation frequency from the ε, α, and β bands of compounds with the indicated Te contents. (g) Axial ratio of the Fermi surface of the α, ε, and β bands as a function of Te content.

There are four dominant frequencies at 5, 21, 124, and 139 T. Three of them are close to the frequencies of F_α (23 T) and F_η (101, 120, 137 T), extracted from SdH oscillations on the same sample. However, there are two major differences between the results of the two kinds of oscillations. The lowest frequency of dHvA oscillations has not been detected in SdH oscillations, and F_ε of SdH oscillations is not observed in dHvA results. SdH oscillations are in concert with the oscillations of the density of states in the vicinity of the Fermi level, while dHvA oscillations originate from the oscillations of the free energy of electrons [41]. Hence, the observed frequencies between SdH and dHvA oscillations could be different due to the difference in probing methods. Similar results were observed in previous reports on ZrSiS crystals [16,41].

The temperature dependence of the FFT amplitude of each frequency is shown in Fig. 6(c), and m^* of each frequency is extracted by using Lifshitz-Kosevich (LK) formula: $R_T = \alpha T m^*/[m_0 B \sinh(\alpha T m^*/m_0 B)]$ [41], where $\alpha = (2\pi^2 k_B m_e)/(\hbar e)$. As shown in Fig. 6(c), m^* of different FS varies from $0.049m_0$ to $0.142m_0$. Thus, Pauli susceptibility $\chi_P = -3(m^*/m_0)^2\chi_O \simeq -0.03\chi_O$, where χ_O is the orbital susceptibility. Therefore, orbital diamagnetism is dominant, and we can neglect the contribution from Pauli paramagnetism.

Figure 6(d) shows the evolution of magnetic susceptibility χ_c as a function of Te content. According to theoretical predictions [46,48], the orbital susceptibility has a negative δ function when the chemical potential ζ approaches critical energies because the system could be considered a sum of 2D gapless systems and, consequently, has diamagnetism with a strong singularity. When ζ crosses these critical energies, the so-called $3\frac{1}{2}$-order electron topological transitions occur in metals [52], which have been experimentally observed in $Na_{1-x}Bi_x$ and BiTeI [49,50]. Here, a Lorentzian representation of the δ function [53],

$$\delta(x) = \lim_{m\to\infty} \frac{1}{\pi}\frac{m}{1+m^2x^2}, \tag{2}$$

is employed to fit the susceptibilities in Fig. 6(d). For $x \leqslant 0.67$, with increasing Te content, diamagnetic susceptibility is enhanced and can be well fitted by Eq. (2) with $m = 3$. The critical point is located around $x = 0.80$. Samples with $x = 0.85$ and ZrSiTe exhibit paramagnetism, in accordance with previous reported results [14]. Clearly, this change in magnetic properties can be related to the anomalies observed in Figs. 2(e) and 3(d), demonstrating an electron topological transition. There are two possible origins for this enhanced paramagnetism observed in samples with $x \geqslant 0.80$. One is

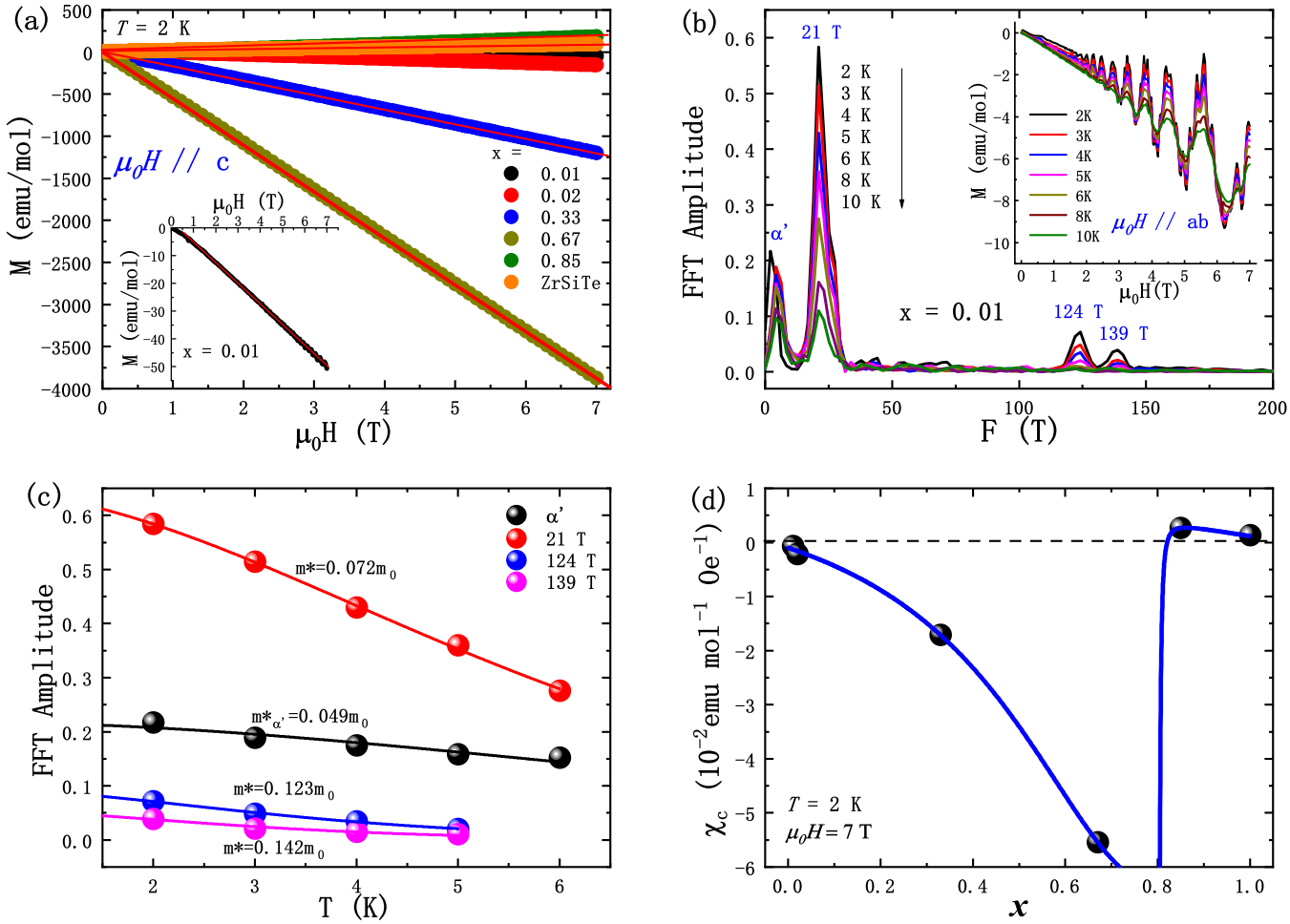

FIG. 6. (a) M versus H of the indicated sample at 2 K with field applied along the c axis. Inset: M vs H data for $ZrSiSe_{0.99}Te_{0.01}$. Solid red lines represent the linear dependence of M versus H. (b) FFT spectra of the oscillatory components of the in-plane magnetization at different temperatures for $ZrSiSe_{0.99}Te_{0.01}$. Inset: dHvA oscillations of in-plane magnetization for $ZrSiSe_{0.99}Te_{0.01}$ at different temperatures. (c) Fits of FFT amplitudes as a function of temperature according to the LK formula: $R_T = \alpha T\mu/[B\sinh(\alpha T\mu/B)]$ [41]. (d) Magnetic susceptibility at 7 T and 2 K as a function of Te content. The solid blue line presents the fits of experimental data by the δ function.

the orbital paramagnetism due to the tilted band crossing, which was proposed in Ref. [49] for the Rashba semiconductor BiTeI. The other is the enhanced SOC arising from Te substitution. According to a previous theoretical study [48], the spin-orbit term of susceptibility for nodal-line semimetals is directly related to the topological surface states, which have a steplike jump at the critical energy corresponding to a significant positive contribution to magnetization; consequently, the system is paramagnetic in total. Furthermore, we did not observe any anomalies in the evolution of carrier densities and mobilities, as seen in Fig. 4, indicating the transition here is a $3\frac{1}{2}$-order one, instead of a $2\frac{1}{2}$-order Lifshitz transition.

IV. SUMMARY

We studied the evolution of FSs in the topological nodal-line semimetal $ZrSiSe_{1-x}Te_x$ by tuning the elemental ratio of chalcogenide elements. For $0.20 \leqslant x \leqslant 0.33$, dramatic changes in the resistivity power law components and the symmetry of AMR indicate a FS topology change. The results of the Hall conductivity analysis showed further evidence through the change in carrier type and mobilities. All the above results suggest that a Lifshitz transition occurs when $0.20 \leqslant x \leqslant 0.33$.

However, for the anomalies shown in the power law components of the resistivity and symmetry of FSs at $x \sim 0.80$, no corresponding change in carrier densities and mobilities was observed. Further investigations of the magnetic properties suggested that the system shows Landau diamagnetism and orbital paramagnetism when x is below and above 0.80, respectively. The diverging diamagnetic susceptibility around $x \sim 0.80$ indicates that the chemical potential ζ crosses a singularity of the electronic band of $ZrSiSe_{0.2}Te_{0.8}$. This singularity could be a band-contacted line or a Dirac node. The orbital paramagnetism observed when $x \geqslant 0.80$ may have two possible mechanisms. One is the tilted Dirac cones in electronic bands, and the other is the enhanced SOC, which may cause a step function distribution of susceptibility at a critical energy, such as a band-contacted line. According to previous theoretical investigation and our results, this transition is a $3\frac{1}{2}$-order electron topological transition.

In summary, we presented the detailed evolution of FSs from ZrSiSe and ZrSiTe. The FS information for $ZrSiSe_{1-x}Te_x$ samples was analyzed by AMR and susceptibility. With increasing x, experimental results showed signatures of FS topology changes in the range of 0.20–0.33 and at ∼0.80, in which the enhanced SOC and charge transfer play crucial roles. These compounds also showed an example with orbital paramagnetism, which could enrich corresponding theoretical investigations. Furthermore, ZrSiM could not only be applied to magnetic sensors in the future but could also provide a better platform to study the tunable topological nodal-line state and the novel properties of topological nodal-line fermions via tuning the chemical potential.

ACKNOWLEDGMENTS

We thank Prof. L. Zou for detailed discussions. This work is supported by the National Key Research and Development Program of China (Grants No. 2016YFA0300404, No. 2017YFA0402100, and No. 2017YFA0402900) and the NSFC (Grants No. U1432138, No. 11474288, and No. 11974354), the Collaborative Innovation Program of Hefei Science Center, CAS (Grant No. 2019HSC-CIP007), and the High Magnetic Field Laboratory of Anhui Province.

[1] L. M. Schoop, M. N. Ali, C. StraBer, A. Topp, A. Varykhalov, D. Marchenko, V. Duppel, Stuart, S. P. Parkin, B. V. Lotsch, and C. R. Ast, Nat. Commun. **7**, 11696 (2016).
[2] D. Takane, Z. Wang, S. Souma, K. Nakayama, C. X. Trang, T. Sato, T. Takahashi, and Y. Ando, Phys. Rev. B **94**, 121108(R) (2016).
[3] C. Bian, T. R. Chang, R. Sankar, S.-Y. Xu, H. Zheng, T. Neupert, C.-K. Chiu, S.-M. Huang, G. Chang, I. Belopolski, D. S. Sanchez, M. Neupane, N. Alidoust, C. Liu, B. Wang, C.-C. Lee, H.-T. Jeng, C. Zhang, Z. Yuan, S. Jia, A. Bansil, F. Chou, H. Lin, and M. Z. Hasan, Nat. Commun. **7**, 10556 (2016).
[4] Y. Wu, L. L. Wang, E. Mun, D. D. Johnson, D. X. Mou, L. Huang, Y. B. Lee, S. L. Budko, P. C. Canfield, and A. Kaminski, Nat. Phys. **12**, 667 (2016).
[5] Q. N. Xu, R. Yu, Z. Fang, X. Dai, and H. M. Weng, Phys. Rev. B **95**, 045136 (2017).
[6] S. M. Young and C. L. Kane, Phys. Rev. Lett. **115**, 126803 (2015).
[7] Z. Zhu, T.-R. Chang, C.-Y. Huang, H. Pan, X.-A. Nie, X.-Z. Wang, Z.-T. Jin, S.-Y. Xu, S.-M. Huang, D.-D. Guan, S. Wang, Y.-Y. Li, C. Liu, D. Qian, W. Ku, F. Song, H. Lin, H. Zheng, and J.-F. Jia, Nat. Commun. **9**, 4153 (2018).
[8] E. Mun, H. Ko, G. J. Miller, G. D. Samolyuk, S. L. Budko, and P. C. Canfield, Phys. Rev. B **85**, 035135 (2012).
[9] E. Emmanouilidou, B. Shen, X. Y. Deng, T. R. Chang, A. Shi, G. Kotliar, S. Y. Xu, and N. Ni, Phys. Rev. B **95**, 245113 (2017).
[10] S. Pezzini, M. R. van Delft, L. M. Schoop, B. V. Lotsch, A. Carrington, M. I. Katsnelson, N. E. Hussey, and S. Wiedmann, Nat. Phys. **14**, 178 (2018).
[11] Y. Huh, E. G. Moon, and Y. B. Kim, Phys. Rev. B **93**, 035138 (2016).
[12] A. A. Burkov, Phys. Rev. B **97**, 165104 (2018).
[13] R. Singha, A. K. Pariari, B. Satpati, and P. Mandal, Proc. Natl. Acad. Sci. U.S.A. **114**, 2468 (2017).
[14] J. Hu, Z. Tang, J. Liu, X. Liu, Y. L. Zhu, D. Graf, K. Myhro, S. Tran, C. N. Lau, J. Wei, and Z. Q. Mao, Phys. Rev. Lett. **117**, 016602 (2016).
[15] M. Matusiak, J. Cooper, and D. Kaczorowski, Nat. Commun. **8**, 152519 (2017).
[16] M. N. Ali, L. M. Schoop, C. Garg, J. M. Lippmann, E. Lara, B. Lotsch, and S. S. P. Parkin, Sci. Adv. **2**, e1601742 (2016).
[17] Y. Y. Lv, B. B. Zhang, X. Li, S. H. Yao, Y. Chen, J. Zhou, S. T. Zhang, M. H. Lu, and Y. F. Chen, Appl. Phys. Lett. **108**, 244101 (2016).
[18] H. Y. Pan, B. B. Tong, J. H. Yu, J. Wang, D. Z. Fu, S. Zhang, B. Wu, X. G. Wan, C. Zhang, X. F. Wang, and F. Q. Song, Sci. Rep. **8**, 9340 (2018).
[19] M. M. Hosen, K. Dimitri, I. Belopolski, P. Maldonado, R. Sankar, N. Dhakal, G. Dhakal, T. Cole, P. M. Oppeneer, D. Kaczorowski, F. Chou, M. Z. Hasan, T. Durakiewicz, and M. Neupane, Phys. Rev. B **95**, 161101(R) (2017).
[20] A. Topp, J. M. Lippmann, A. Varykhalov, V. Duppel, B. V. Lotsch, C. R. Ast, and L. M. Schoop, New J. Phys. **18**, 125014 (2016).
[21] L. Tian, Y. Liu, W. Z. Meng. X. M. Zhang. X. F. Dai, and G. D. Liu, J. Phys. Chem. Lett. **11**, 10340 (2020).
[22] T. Zhou, M. Y. Tong, X. N. Xie, Y. Y. Yu, X. G. Zhu, Z. Y. Wang, and T. Jiang, J. Phys. Chem. Lett. **11**, 6475 (2020).
[23] I. M. Lifshitz, Sov. Phys. JETP **11**, 1130 (1960).
[24] A. Martin-Ruiz and A. Cortijo, Phys. Rev. B **98**, 155125 (2018).
[25] F. C. Chen, Y. Fei, S. J. Li, Q. Wang, X. Luo, J. Yan, W. J. Lu, P. Tong, W. H. Song, X. B. Zhu, L. Zhang, H. B. Zhou, F. W. Zheng, P. Zhang, A. L. Lichtenstein, M. I. Katsnelson, Y. Yin, N. Hao, and Y. P. Sun, Phys. Rev. Lett. **124**, 236601 (2020).
[26] R. Juneja, R. Shinde, and A. K. Singh, J. Phys. Chem. Lett. **9**, 2202 (2018).
[27] P. Dziawa, B. J. Kowalski, K. Dybko, R. Buczko, A. Szczerbakow, M. Szot, E. Łusakowska, T. Balasubramanian, B. M. Wojek, M. H. Berntsen, O. Tjernberg, and T. Story, Nat. Mater. **11**, 1023 (2012).
[28] S. Y. Xu *et al.*, Nat. Commun. **3**, 1192 (2012).
[29] G. P. Mikitik and Yu. V. Sharlai, J. Low Temp. Phys. **197**, 272 (2019).
[30] P. Blaha, K. Schwarz, G. K. H. Madsen, D. Kvasnicka, J. Luitz, R. Laskowski, F. Tran, and L. D. Marks, *WIEN2k, an Augmented Plane Wave plus Local Orbitals Program for Calculating Crystal Properties*, Karlheinz Schwarz (Technische Universität Wien, Vienna, 2001).
[31] J. P. Perdew, K. Burke, and M. Ernzerhof, Phys. Rev. Lett. **77**, 3865 (1996).
[32] C. Wang and T. Hughbank, Inorg. Chem. **34**, 5524 (1995).
[33] See Supplemental Material at http://link.aps.org/supplemental/10.1103/PhysRevB.103.165141 for single crystal characterization, magnetoresistance data of all samples and additional FFT analyses of SdH oscillations, dHvA oscillations for $x < 0.33$.
[34] R. J. Goetsch, V. K. Anand, A. Pandey, and D. C. Johnston, Phys. Rev. B **85**, 054517 (2012).

[35] R. Sankar, G. Peramaiyan, I. Panneer Muthuselvam, C. J. Butler, K. Dimitri, M. Neupane, G. N. Rao, M.-T. Lin, and F. C. Chou, Sci. Rep. **7**, 40603 (2017).
[36] N. Kumar, C. Shekhar, S. C. Wu, I. Leermakers, O. Young, U. Zeitler, B. Yan, and C. Felser, Phys. Rev. B **93**, 241106(R) (2016).
[37] S. Sun, Q. Wang, P. J. Guo, K. Liu, and H. Lei, New J. Phys. **18**, 082002 (2016).
[38] G. Blatter, V. B. Geshkenbein, and A. I. Larkin, Phys. Rev. Lett. **68**, 875 (1992).
[39] O. Pavlosiuk, P. Swatek, and P. Wisniewski, Sci. Rep. **6**, 38691 (2016).
[40] O. Pavlosiuk, M. Kleinert, P. Swatek, D. Kaczorowski, and P. Wisniewski, Sci. Rep. **7**, 12822 (2017).
[41] J. Hu, Z. J. Tang, J. Y. Liu, Y. L. Zhu, J. Wei, and Z. Q. Mao, Phys. Rev. B **96**, 045127 (2017).
[42] Q. Chen, Z. F. Lou, S. N. Zhang, B. J. Xu, Y. X. Zhou, H. C. Chen, S. J. Chen, J. H. Du, H. D. Wang, J. H. Yang, Q. S. Wu, O. V. Yazyev, and M. H. Fang, Phys. Rev. B **102**, 165133 (2020).
[43] M. N. Ali, J. Xiong, S. Flynn, J. Tao, Q. D. Gibson, L. M. Schoop, T. Liang, N. Haldolaarachchige, M. Hirschberger, N. P. Ong, and R. J. Cava, Nature (London) **514**, 205 (2014).
[44] T. I. Sigfusson, K. P. Emilsson, and P. Mattocks, Phys. Rev. B **46**, 10446 (1992).
[45] C. Q. Xu, Y. Liu, P. G. Cai, B. Li, W. H. Jiao, Y. L. Li, J. Y. Zhang, W. Zhou, B. Qian, X. F. Jiang, Z. X. Shi, R. Sankar, J. L. Zhang, F. Yang, Z. W. Zhu, P. Biswas, D. Qian, X. L. Ke, and X. F. Xu, J. Phys. Chem. Lett. **11**, 7782 (2020).
[46] G. P. Mikitik and Yu. V. Sharlai, Phys. Rev. B **94**, 195123 (2016).
[47] G. P. Mikitik and Yu. V. Sharlai, Phys. Rev. B **97**, 085122 (2018).
[48] M. Koshino and I. F. Hizbullah, Phys. Rev. B **93**, 045201 (2016).
[49] E. Röber, K. Hackstein, H. Coufal, and S. Sotier, Phys. Status Solidi B **93**, K99 (1979).
[50] G. A. H. Schober, H. Murakawa, M. S. Bahramy, R. Arita, Y. Kaneko, Y. Tokura, and N. Nagaosa, Phys. Rev. Lett. **108**, 247208 (2012).
[51] C. G. Wang, Y. Honjo, L. X. Zhao, G. F. Chen, K. Matano, R. Zhou, and G. Q. Zheng, Phys. Rev. B **101**, 241110(R) (2020).
[52] G. P. Mikitik and Yu. V. Sharlai, Phys. Rev. B **90**, 155122 (2014).
[53] R. P. Kanwal, *Generalized Functions: Theory and Applications*, 3rd ed. (Springer, New York, 2004).